Journal of Colloid and Interface Science 628 (2022) 407–418

Contents lists available at ScienceDirect

Journal of Colloid and Interface Science

journal homepage: www.elsevier.com/locate/jcis

Enhancing cyclic and in-air stability of Ni-Rich cathodes through perovskite oxide surface coating

Peiyuan Guan [a], Yanzhe Zhu [a], Mengyao Li [a], Tianyi Zeng [b], Xiaowei Li [b], Ruoming Tian [c], Neeraj Sharma [d], Zhemi Xu [e], Tao Wan [a,*], Long Hu [a], Yunjian Liu [b,*], Claudio Cazorla [f,*], Dewei Chu [a]

[a] School of Materials Science and Engineering, University of New South Wales, Sydney 2052, Australia
[b] School of Material Science and Engineering, Jiangsu University, Zhenjiang 212013, PR China
[c] Solid State & Elemental Analysis Unit, University of New South Wales, Sydney 2052, Australia
[d] School of Chemistry, University of New South Wales, Sydney 2052, Australia
[e] Chemistry and Material Engineering College, Beijing Technology and Business University, Beijing 100048, PR China
[f] Departament de Física, Universitat Politècnica de Catalunya, Campus Nord B4-B5, E-08034 Barcelona, Spain

GRAPHICAL ABSTRACT

In this work, STO-coated NCM811 cathode materials were obtained through a facile wet chemical method, exhibiting excellent cyclic stability. Additionally, the STO-coated NCM811 could also mitigate the Li_2CO_3 generation on the cathode surface by effective isolation from H_2O and CO_2. Thus, higher specific capacity was retained after long-term storage in the air compared to the uncoated NCM811 sample. Our studies proposed an effective surface modification strategy to enhance the electrochemical performance of layered ternary oxides for high performance-cathodes in commercial LIBs.

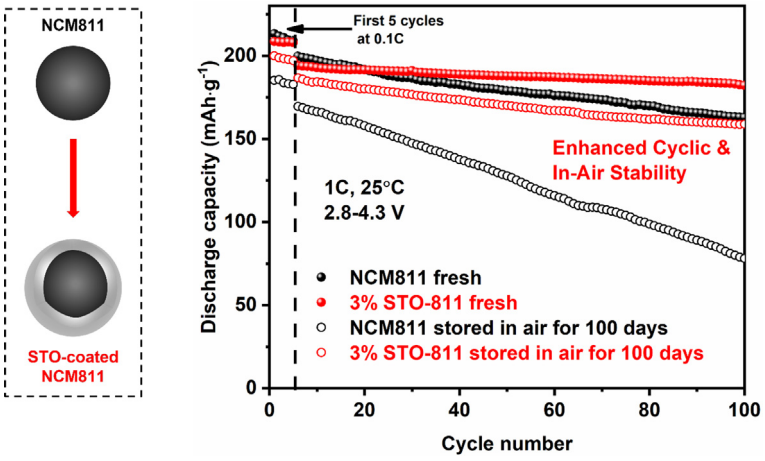

ARTICLE INFO

Article history:
Received 11 July 2022
Revised 8 August 2022
Accepted 10 August 2022
Available online 13 August 2022

ABSTRACT

Ni-rich layered oxides, such as $LiNi_{0.8}Co_{0.1}Mn_{0.1}O_2$ (NCM811), are promising cathode materials for high-energy lithium-ion batteries. However, the relatively high reactivity of Ni in NCM811 cathodes results in severe capacity fading originating from the undesired side reactions that occur at the cathode-electrolyte interface during prolonged cycling. Therefore, the trade-off between high capacity and long cycle life can obstruct the commercialization process of Ni-rich cathodes in modern lithium-ion batteries (LIBs). In

* Corresponding authors.
E-mail addresses: tao.wan@unsw.edu.au (T. Wan), lyjian122331@163.com (Y. Liu), claudio.cazorla@upc.edu (C. Cazorla).

https://doi.org/10.1016/j.jcis.2022.08.061

Keywords:
Lithium-ion battery
Ni-rich cathode
Surface modification
Cycling performance enhancement
In-air storage stability

addition, high sensitivity toward air upon storage greatly limits the commercial application. Herein, a facile surface modification strategy is introduced to enhance the cycling and in-air storage stability of NCM811. The NCM811 with a uniform $SrTiO_3$ (STO) nano-coating layer exhibited outstanding electrochemical performances that could deliver a high discharge capacity of 173.5 $mAh{\cdot}g^{-1}$ after 200 cycles under 1C with a capacity retention of 90%. In contrast, the uncoated NCM811 only provided 65% capacity retention of 130.8 $mAh{\cdot}g^{-1}$ under the same conditions. Structural evolution analysis suggested that the STO coating acted as a buffer layer to suppress the dissolution of transition metal ions caused by the HF attack from the electrolyte and promote the lithium diffusion during the charge–discharge process. In addition, the constructed STO layer prevented the exposure of NCM811 to H_2O and CO_2 and thus effectively improved the in-air storage stability. This work offers an effective way to enhance the performance stability of Ni-rich oxides for high-performance cathodes of lithium-ion batteries.

1. Introduction

The ever-increasing demand for energy storage in electric vehicles (EVs) has triggered the development of high-energy–density LIBs with reliable and long cycling life. As an essential component of LIBs, the cathode material determines the performance of the batteries, including energy density, safety, and service life. Among various cathode materials, $LiNi_{0.8}Co_{0.1}Mn_{0.1}O_2$ (NCM811), a typical Ni-rich cathode material, has received enormous research interest in recent years on account of its high theoretical capacity (~280 $mAh{\cdot}g^{-1}$), high energy density (~800 $Wh{\cdot}kg^{-1}$), low cost, and environmental friendliness [1–4].

However, several challenges still limit widespread practical use in energy storage applications. For instance, with the increasing Ni content in the layer-structured cathode materials, cation mixing between Li^+ and Ni^{2+} becomes severe during the lithiation/delithiation process due to the similar ionic radius. Li/Ni mixing would not only generate 'dead Li' aggravating the capacity decay of NCM811 but also trigger surface reconstructions of the material, resulting in irreversible phase transitions (layered to rock-salt), further blocking the Li diffusion pathway [5–7]. In addition, although the Ni^{3+}/Ni^{4+} couple leads to a high discharge capacity, especially at high cut-off voltage, side reactions of highly reactive Ni^{4+} promote the dissolution of transition metal (TM) ions into the organic electrolyte, accompanied by oxygen loss from the cathode crystal structure during long-term cycling. Structural degradations deriving from these unfavourable effects bring about poor cyclability and safety issues for NCM811 [8–10]. Furthermore, lithium residues ($LiOH/Li_2CO_3$) from synthesis or storage on the cathode surface that are moisture-absorbing are responsible for the $LiPF_6$ electrolyte decomposition, further causing corrosive HF generation. The generated HF would attack the bare cathode particles to create an insulating LiF layer, regarded as the cathode-electrolyte interphase (CEI), resulting in sluggish Li transfer kinetics in NCM811 [11–13].

Based on our previous review work, the surface modification strategy has been widely applied to address these challenges because of its relatively simple process and rare influence on the core materials [14]. Despite many types of materials (e.g., oxides, fluorides, and phosphates) that have been employed as coating layers onto layer-structured oxide cathodes, perovskite-based coating materials have barely been investigated. As a model example, $SrTiO_3$ (STO) nanomaterials with excellent stability and unique defect chemistry plays a significant role in solid-state research [15].

Herein, we introduce STO nanoparticles into the Ni-rich cathode system as a coating material for the first time to verify their functionality. The characterization and electrochemical measurement results have demonstrated that the STO nano-coating could efficiently protect NCM811 from undesired side reactions with the electrolyte. Severe phase transitions that cause microcrack generation inside the cathode particles during long-term Li^+ intercalation/deintercalation appears to be avoided. By optimizing the mass ratio of coated STO, the cycling performance of NCM811 is improved. The outcomes demonstrate that the 3 wt% STO-coated NCM811 delivers a discharge capacity of 173.5 $mAh{\cdot}g^{-1}$ after 200 cycles under 1C in the potential range of 2.8–4.3 V with a capacity retention of 90 %. Besides, after a long period of storage (100 days) under ambient conditions (room temperature ~ 25 ℃ and relative humidity ~ 40 %), all cathode materials (with and without STO coated NCM811) show worse electrochemical performances compared to those stored in Ar-filled glovebox. However, the STO coated electrodes show relatively higher capacity and lower voltage decay than pristine NCM811. This study reveals the effective protection of NCM811 particles from direct contact of the electrolyte to eliminate side reactions.

2. Experimental section

2.1. Materials preparation

The NCM811 was purchased from the Hubei Jiangchen New Energy Technology Co. ltd., and other raw materials were obtained from Sigma-Aldrich. All chemicals were utilized as received without additional purification. The STO nanoparticles were synthesized by a solvothermal assisted hydrolysis process [16]. In a typical synthesis of STO, equimolar of $Sr(OH)_2{\cdot}8H_2O$ (95 %) and tetrabutyl titanate ($Ti(OBu)_4$) solution (97 %) were dissolved into triethylene glycol (TEG: 99 %) under vigorous stirring. Afterwards, 5 mL of ammonia solution (27 wt% in H_2O) and 0.6 g of polyvinylpyrrolidone (PVP) (Mw ~ 40,000) were added to the solution. Then, the total volume of the mixture was adjusted to 30 mL, and the resultant solution was then transferred and sealed into an autoclave by gradually heated up to 160 ℃ for 4 h. After cooling to room temperature, the obtained sol was separated using D.I. water to precipitate the nanoparticles. Finally, the as-prepared STO nanoparticles were washed with D.I. water and absolute ethanol several times to remove soluble impurities and dried at 80 ℃ for further coating.

STO-coated NCM811 was obtained through a facile wet chemical coating method. Purchased NCM811 powder and STO powder were weighed with various ratios and poured into a beaker containing 100 mL of absolute ethanol. Then, the mixture was magnetically stirred till the solvent completely evaporated. After drying the pre-coated powders at 80 °C for 12 h, the samples were annealed in air at 400 °C for 6 h to obtain the final products. According to the weight percentage of added STO nanoparticles (1 wt%, 3 wt% and 5 wt%) in the coating process, the obtained samples were labelled as 1 %, 3 %, and 5 % STO-811, respectively.

2.2. Characterization

The X-ray diffraction (XRD) data were collected from the PANalytical Xpert Multipurpose XRD System under 45 kV and 40 mA

operating conditions. Basic Rietveld refinements were conducted on the HighScore Plus software (version 4.9). The morphology of the particles was captured using a field-emission scanning electron microscope (NanoSEM 450). High-resolution transmission electron microscope (HRTEM) images were observed using the JEOL JEM-F200 scanning transmission electron microscope (STEM) with a cold field emission gun (FEG). The energy-dispersive X-ray spectroscopy (EDS) data were obtained using a FEI Tecnai G2 20 instrument. The X-ray photoelectron spectroscopy (XPS) data were collected using an ESCALAB250Xi instrument (Thermo Scientific, UK) operating at 120 W. C 1 s = 284.8 eV was used for the Binding energy reference for all XPS spectra. In the case of the post-mortem examination, the cycled cells were immediately transferred to the glovebox for disassembling. The cycled cathodes were washed with DMC to remove electrolyte residue adhered to the cathode surface and left for 24 h to allow DMC evaporation. The focused ion beam (FIB) technique was employed to detect the microcracks inside of cathode spherical particles utilising the ThermoFisher Helios G4 PFIB UXe DualBeam system (2.5μA Xe plasma FIB ion).

2.3. Electrochemical measurement

All the electrochemical measurements were conducted using coin type half-cells manufactured in an Ar-filled glovebox (H_2O and O_2 less than 0.5 ppm). In detail, cathodes were firstly fabricated by mixing 80 wt% active materials, 10 wt% acetylene black conductive agent, and 10 wt% polyvinylidene fluoride (PVDF) binder. Afterwards, an appropriate amount of *n*-methyl-2-pyrrolidone (NMP) was added to the mixture powder, and then the collected slurry was uniformly cast onto Al foil. After drying at 120 ℃ for 12 h, as-prepared cathodes with the loading mass of active material were 2.5–3.5 mg·cm^{-2}. CR2032 coin cells were assembled in the glovebox with Li metal as the anode, polypropylene (Celgard 2400) as the separator, and 1 M $LiPF_6$ dissolved in a mixture of ethylene carbonate and dimethyl carbonate (EC: DMC = 1:1 in volume) as the electrolyte. All the electrochemical measurements were performed at room temperature, and each cell was rested for 12 h before a galvanostatic charge. The cyclability and rate performance were measured on a NEWARE battery test system, and the dQ/dV spectra were also directly extracted from the NEWARE cycler. The cyclic voltammogram (CV) and electrochemical impedance spectra (EIS) with a 10^{-2}-10^5 Hz frequency range were obtained on an Autolab PGSTAT302N electrochemical workstation.

3. Results and discussion

3.1. Structural analysis

The XRD and TEM characterizations of as-synthesized STO are shown in **Figure S1** (Supplementary). All diffraction peaks index to perovskite STO without any impurities, and the TEM images reveal the nanocubes morphology of STO particles with an average size of ~ 20 nm. Moreover, the d-spacing measured from HRTEM is 2.79 Å, corresponding to the (110) crystalline plane of STO. XRD patterns depicted in Fig. 1**(a) and (b)** clearly show that the pristine and the coated NCM811 can be indexed to the *R*-3 *m* space group (Peaks are labelled correspondingly). In particular, Fig. 1**(b)** shows the enlarged XRD curves from 31 to 39 (2θ degree), in which apparent STO reflection peaks can be observed after the coating content increased to 5 %. The other coated samples exhibit high crystallinity of NCM811 without additional phases due to the relatively low STO quantity and nanosized morphology. It still should point out that a bump was detected at 32.3° (index to STO additive) in the XRD result of 3 % STO-811, which is too tiny to be seen clearly in Fig. 1**(a) and (b)**. In addition, the observed splitting of (006)/(012) and (018)/(110) indicate a well-ordered α-$NaFeO_2$-like layered structure, suggesting that the STO nanocoating barely affects the structure of Ni-rich cathode [17].

Rietveld refinements were employed to explore the layered structure of the STO-coated NCM811. All R_{wp} values are below 5 %, confirming the trustworthy outcomes (Rietveld analysis details are shown in **Figure S2 and Table S1**). It can be obtained from **Table S2** that the crystal parameters 'a' and 'c' demonstrate insignificant changes before and after STO coating, inferring that the STO additive is solely coated outside of the NCM811 particles without structure degradation of Ni-rich cathodes or ionic substitutions between cathode materials and coating materials. It is rational because the annealing temperature applied after the wet-chemical coating process is relatively low (400℃), which may not be enough to trigger potential ion drifting at the cathode-coating interfaces. Thus, this work will focus on the sole coating effect of STO for Ni-rich NCM811 cathode. For higher temperature thermal treatment induced potential element doping or interphase formation will be investigated in our further work.

Generally, the c/a ratio of the octahedral MO_6 (M = Ni, Co, Mn) can be regarded as an indicator to reveal the orderliness of the crystal structure [18], and the values are found to be higher than 4.9 in this work, confirming that the surface-modified NCM811 materials preserved their original layered structure. Moreover, the peak intensity ratio between the (003) and (104) implies the Li/Ni disordering degree, (i.e., Li and Ni site mixing on the 3*a* and 3*b* crystallographic sites) resulting from the similar ionic radius between Li^+ (0.76 Å) and Ni^{2+} (0.69 Å) [19]. When the I_{003}/I_{104} ratio is higher than 1.2, it reflects a well-ordered crystal phase with a low percentage of Li/Ni disorder, and all the samples in this work are ~ 1.28, suggesting an ordered structure (minimal Li/Ni site mixing).

Fig. 1**(c)** illustrates the SEM images of pristine NCM811, in which a spherical structure of secondary particles with a diameter range of 8–15 μm is noted. The insert SEM image exhibits the secondary sphere composed of numerous nano-scaled primary particles with smooth surfaces. Fig. 1**(d-f)** show the secondary particles of STO coated cathode material, all of which maintain the spherical morphology. However, the particle surface becomes rougher after the coating. The SEM-EDS mapping results of 1 %, 3 % and 5 % STO-811 are displayed in **Figure S3**, confirming that the STO has been successfully coated onto the cathode particles. Nevertheless, when the coating ratio increased to 5 %, inhomogeneous coating parts appeared, which may be due to the Ostwald ripening under heat treatment [20].

Pristine NCM811 displays a smooth surface, and lattice spacings of 4.73 Å are observed, corresponding to the (003) crystal plane of NCM811 (Fig. 2**(a)**). What appears to be a coating layer can be seen on the surface of the particles. Qualitatively, the layer thickness appears to increase with increasing STO content, as shown in the insets of Fig. 2**(b-d)**. Clear lattice fringes of STO corresponding to the (200) crystal plane are noted, and more crystal facets are discernible as the STO content is increased. This proves STO is on the NCM811 particles surface and both NCM811 and STO don't change their structure within the resolution afforded and techniques used. TEM-EDS mapping of 3 % STO-811 (**Figure S4**) demonstrates Sr and Ti distribution over the particle. It should be noted that the 1 % STO-811 reveals some uncovered sections of the NCM811 particles while the 5 % STO-811 exhibits protruding areas (inset of Fig. 2**(d)**) both presumably due to the STO content added. These data suggest that STO coats the surface, the coating doesn't appear to be perfectly uniform but does appear to coat the majority (if not all) of the NCM811 surfaces examined, with the 3 % STO appearing to show the most consistent coating.

XPS is utilized in this work to determine the surface alterations of NCM811 before and after STO modification. XPS survey profiles

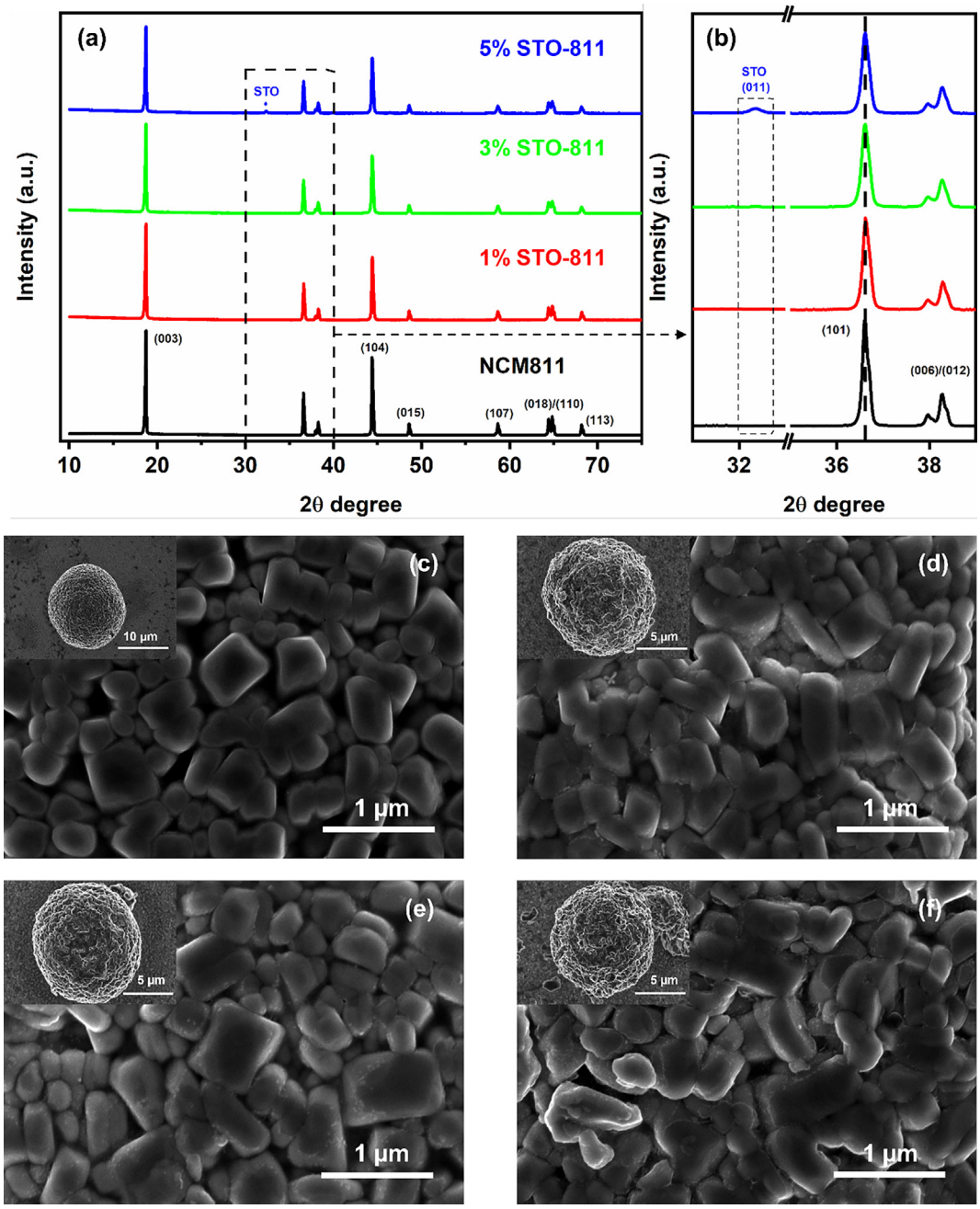

Fig. 1. (a) XRD patterns of NCM811, 1, 3, and 5 wt% STO coated NCM811. (b) enlarged XRD curves of all samples. SEM images of (c) NCM811, (d) 1% STO-811, (e) 3% STO-811, and (f) 5% STO-811.

of all samples are expressed in **Figure S5**. Among them, Ni 2p, Co 2p, Mn 2p, O 1 s, C 1 s, and Li 1 s peaks could be observed in all profiles, while Ti 2p and Sr 3d peaks could be only found in the STO coated samples, which is rational to deduce that STO is successfully coated on the NCM811. The semi-quantitative concentration of Ni^{2+} and Ni^{3+} are calculated by analysing the integration area of the Ni 2p peaks fitted by XPSpeak41 software (Fig. 3**(a)**). The surface Ni^{2+} content of pristine NCM811 is the lowest (21.7 %). All STO-coated cathode materials indicate increased Ni^{2+} ratio of 1 wt% (44.8 %), 3 wt% (25.6 %), and 5 wt% (27.8 %), respectively. Though the increased Ni^{2+} content after STO coating may lead to a higher Li/Ni mixing probability (consistent with the XRD Rietveld refinement results in **Table S1**), 3 % STO-811 exhibits the lowest Ni^{2+} growth in all STO-coated cathode samples. This phenomenon can be explained that a proper STO coating amount may offset the drawback of heating-induced Ni^{2+} generation due to the good thermal resistance of STO [21]. Generally, the thermal treatment can induce the structural disorder of a high-nickel contained layered-structure cathode. In detail, the post-annealing promoted the decomposition of oxygen lattice to form oxygen vacancies. Electrons lost from O^{2-} would be obtained by that dominant Ni^{3+} (e.g., $LiNiO_2$) in the Ni-rich cathode to produce more Ni^{2+}, which can easily migrate into the Li slab, leading to severe Li/Ni disorder [22]. In this case, Ni-rich oxides need to be synthesized under a high O2 atmosphere instead of air for other ternary layered cathode materials to minimize the lattice oxygen loss during high-temperature sintering [23]. Wang et al. found an optimum annealing temperature at around 400 °C for Ni-rich cathodes, effectively reducing the cation mixing degree of NCM811 [24]. That is also the reason we choose 400 °C to prepare samples. Besides,

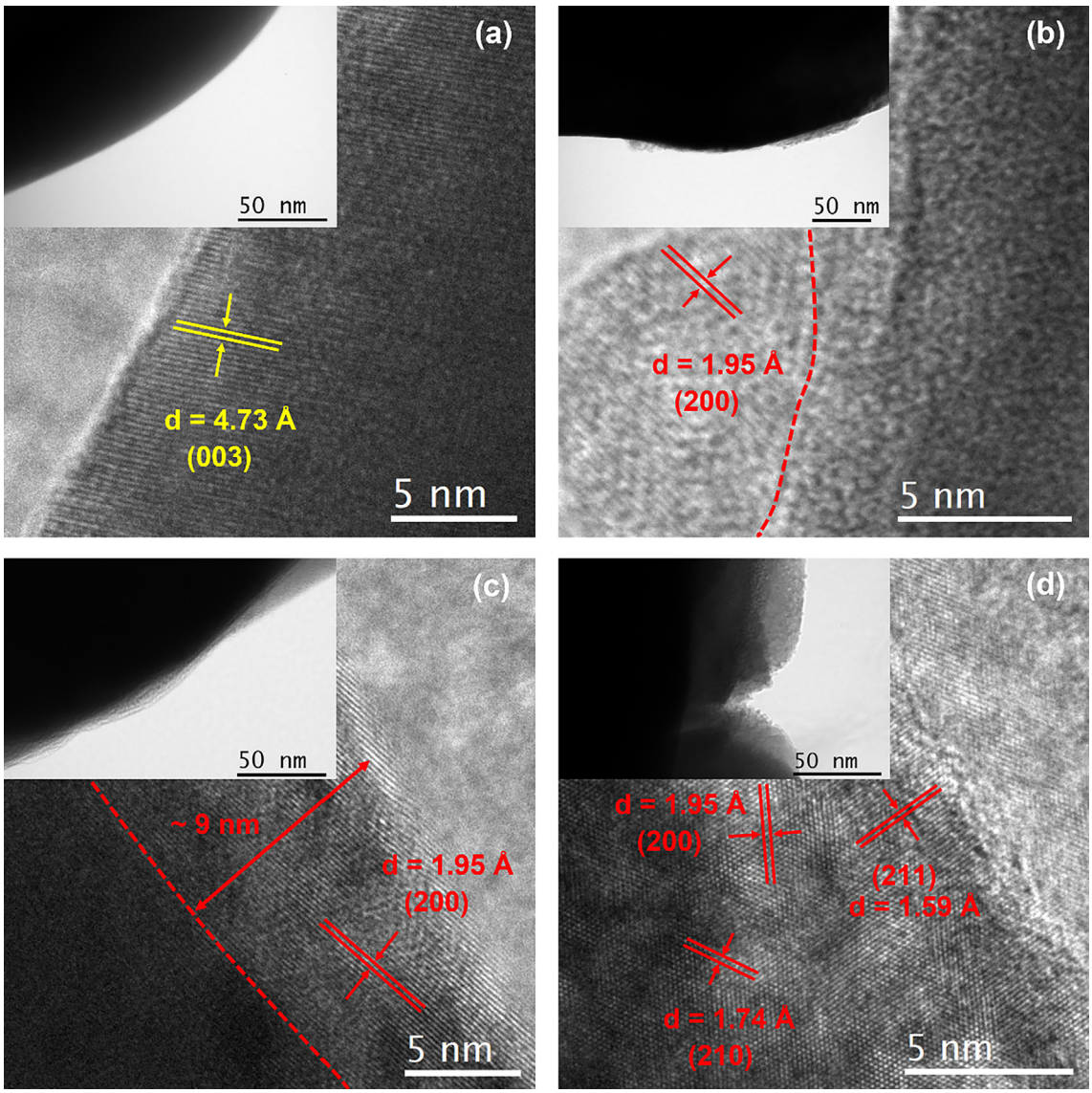

Fig. 2. HRTEM images of (a) pristine NCM811, (b) 1% STO-811, (c) 3% STO-811, and (d) 5% STO-811. The insets show the low magnification TEM images of the cathode materials.

the decreasing of the Ni^{3+} proportion in the Ni-rich material will benefit its in-air storage stability. The Jahn–Teller active Ni^{3+} species are prone to react with H_2O and CO_2 in air and lead to the generation of high-active oxygen, which would induce the formation of $LiOH/Li_2CO_3$ on the surface of cathode materials, further triggering capacity loss during cycling [25,26]. Compared to 1 % STO-811, 5 % STO-811 also shows much lower Ni^{2+} content. Two possible reasons are proposed here: (1) The XPS technique is surface-sensitive, and the 5 % STO coating layer is relatively thick on the NCM811 surface (as illustrated in electron microscope images), making it difficult to precisely determine the Ni^{2+} ratio. However, the thicker coating layer reduces the Ni concentration on the sample surface, which may further suppress the side reactions between organic electrolyte and the oxidized Ni^{4+} after charging [27]. (2) The lower surface Ni^{2+} ratio in 5 % STO-811 may also attribute to the more extensive Ti^{4+} existence at the interface between coating and cathode materials when compared with 1 % STO-811 [28]. Because Ti^{4+} in STO may attract electrons from Ni^{2+} to generate $Ti^{(4-x)+}$ ($0 < x \leq 1$) at the cathode-coating interface due to the higher electronegativity of Ti^{4+} (~2.02) than Ni^{2+} (~1.47), and then raise the valence of Ni from + 2 to + 3 [29]. The likelihood will be further discussed in the Ti 2p XPS profiles analysis.

Co 2p and Mn 2p XPS spectra for all as-prepared cathode samples are also depicted in **Figure S5**. They all disclose a similar peak shape and binding energy, inferring that STO coating barely influences the chemical compositions of the NCM811 cathode surface. O 1 s XPS patterns are demonstrated in Fig. 3**(b)**. The binding energy of ~ 531.5 eV refers to the lattice oxygen in the Ni-rich oxide cathodes that existed in all samples [30]. The newly emerged peak located at ~ 529.3 eV indicates the lattice oxygen of STO, which agrees well with the previous STO XPS investigation [31]. The NCM811-related oxygen peaks are well-aligned with each other, suggesting the XPS results are calibrated and reliable. Furthermore, it is reasonable that the intensity of STO-related oxygen peaks grows with the increase of STO additive amount, confirming the establishment of a thicker coating layer with more STO feeding.

Fig. 3**(c) and (d)** exhibits the Ti 2p and Sr 3d peaks of the STO-coated NCM811, respectively. The binding energy of Ti 2p in 3 % and 5 % STO-811 shifted toward the lower field compared with 1 % STO-811, indicating that the Ti^{4+} received electrons when

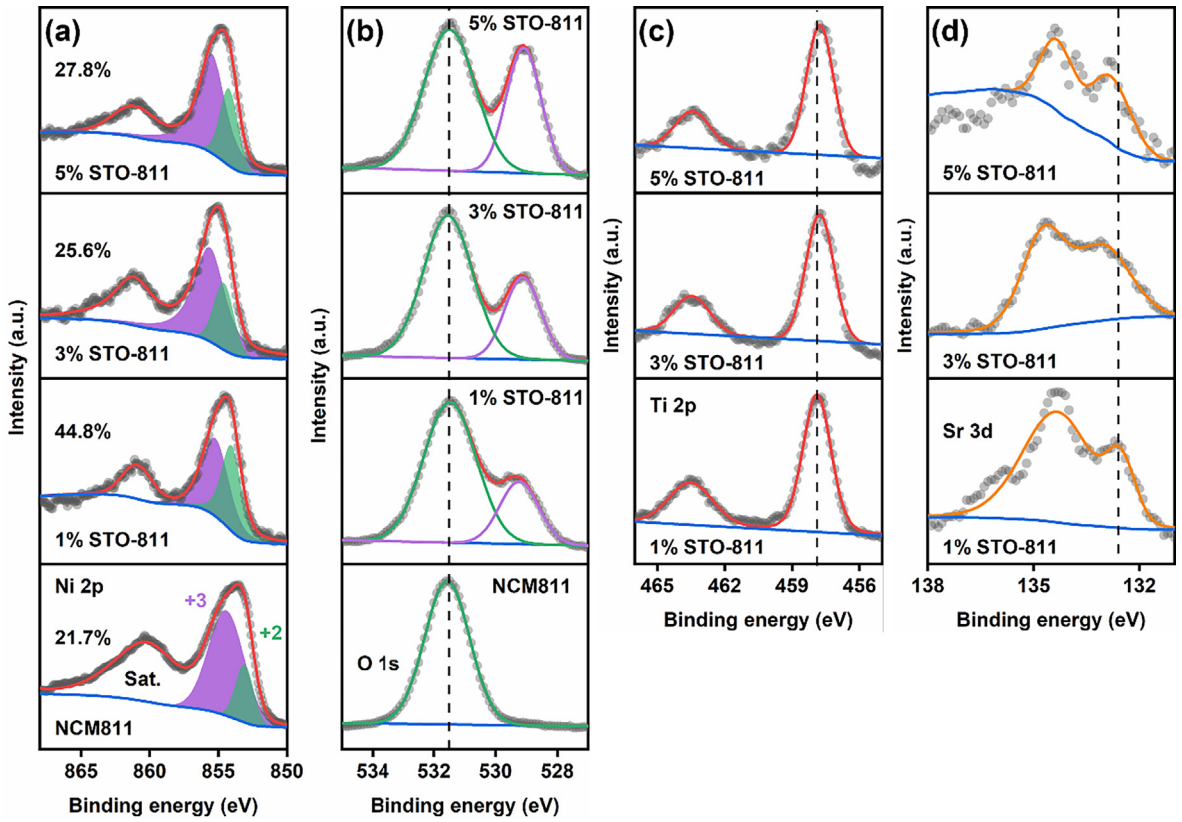

Fig. 3. XPS spectra of (a) Ni 2p and (b) O 1 s for all as-prepared samples. XPS spectra of (c) Ti 2p and (d) Sr 3d for STO-coated NCM811 samples.

higher STO content contacts with the cathode surface [32]. Correspondingly, the bonded Sr 3d peaks shifted to higher binding energies for charge balance. These observations may be regarded as proof of the aforementioned Ni^{2+} ratio decreasing caused by electron competing between Ti^{4+} and Ni^{2+}. However, direct evidence is still required, and an in-depth study will be conducted in our further work. Another expected reason for the electron shift is that trace amount of Li-Ti-O (LTO) compounds (such as $LiTiO_2$) form at the NCM811 and STO interface layer due to the presence of residual Li contaminating the surface of Ni-rich oxide materials after synthesis. The establishment of fast Li^+ conductor LTO in the 3 % STO-811 may actually act to improve the rate performance of the Ni-rich cathode materials [33].

3.2. Electrochemical performance

Fig. 4**(a)** reveals the initial charge–discharge curves of pristine, 1 %, 3 %, and 5 % STO-coated NCM811 under 0.1C (1C = 200 $mA{\cdot}g^{-1}$) and is summarised in Table 1. Not surprisingly, the pristine NCM811 shows the highest initial discharge capacity (214.9 $mAh{\cdot}g^{-1}$) among all the tested half cells, and the 1 % STO-811 demonstrates a slightly decreased capacity of 213.7 $mAh{\cdot}g^{-1}$. Because of the inactive nature of STO, the addition of STO will reduce the effective mass of the active cathode material, resulting in a lower specific capacity. 3 % STO-811 exhibits a relatively low initial specific capacity of 207.3 $mAh{\cdot}g^{-1}$, but its initial Coulombic efficiency is the highest (~92 %) among the samples, which indicates excellent Li^+ intercalation/deintercalation reversibility. The cyclic performance was measured under 1C at room temperature after five stabilization charge–discharge cycles at 0.1C. The discharge capacity retentions of 1 %, 3 %, and 5 % STO-811 are 71.5 %, 89.8 %, and 83.2 %, respectively, which are all better than that of bare NCM811 (65.3 %). Compared with other samples, the capacity loss of 3 % STO-811 is only ~ 0.1 $mAh{\cdot}g^{-1}$ per cycle (Fig. 4**(b) and** Table 1), revealing a more stable cyclability. A long-term cycling measurement of pristine NCM811 and 3 % STO-811 was also conducted at 0.5C at a voltage range of 2.8–4.3 V, as shown in **Figure S6**. After 700 times of repeated charge–discharge, 3 % STO-811 still maintained more than 50 % of its initial discharge capacity (from 204.8 $mAh{\cdot}g^{-1}$ to 104.4 $mAh{\cdot}g^{-1}$), while the discharge capacity of uncoated NCM811 dropped below 100 $mAh{\cdot}g^{-1}$ in less than 500 cycles. All these results support that the optimized amount (3 %) of STO nanocoating could create a uniform layer around the cathode materials without influencing their electrochemical reactions during charge–discharge cycles. In the meantime, the inherent stability of STO would suppress the side reactions between electrolyte and NCM811, which effectively improved the cyclic stability and further prolonged the lifespan of coin cells. Therefore, the electrochemical reversibility and stability of NCM811 are greatly enhanced by STO surface modification, confirming that this facile strategy is conducive to improve the reversible capacity of the Ni-rich oxide cathodes.

Discharge under high current densities isa typical challenge for Ni-rich layered oxide cathodes because the fast delithiation can activate the phase transition from the layered structure to the rock-salt phase. The electrochemical inactive rock-salt phase further hinders the reaction kinetics, causing rapid capacity decay [34]. To clarify that the STO coating may alleviate the phase transformation under high-rate discharge, the rate performance of all the samples is studied, and the results are shown in Fig. 4**(c)**. All the cells were charged at 0.1C with a constant current/constant voltage (CC/CV) model. Then, galvanostatic discharge under various rates from 0.1C to 10C, and finally back to 0.1C was conducted to verify their capacity retention capabilities. The same trends with the cycling test in the low C-rate (≤1C) were observed, while the

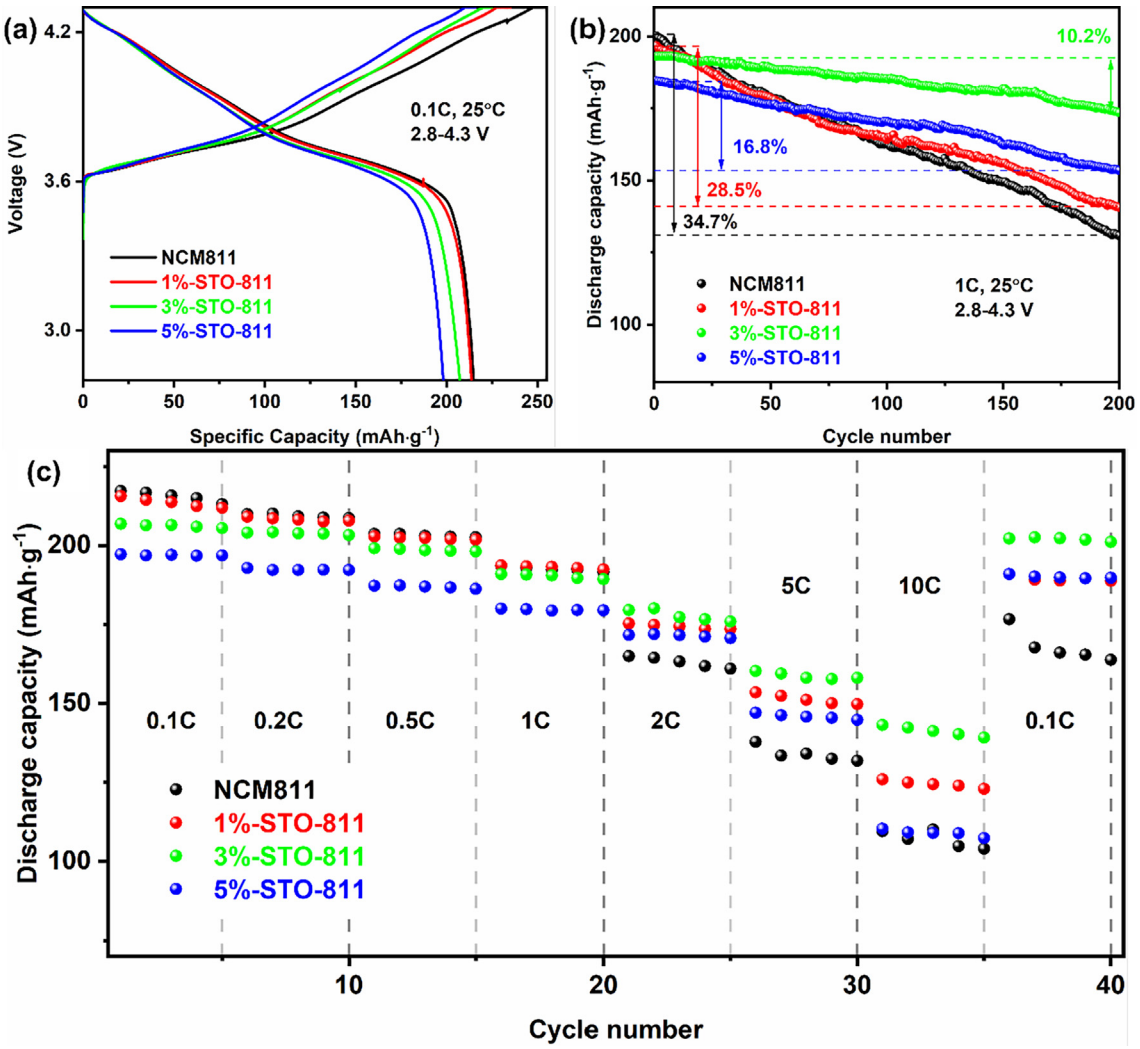

Fig. 4. (a) Initial charge–discharge profile of all samples at 0.1C. (b) Cyclic performances of uncoated and STO coated NCM811 at 1C. The arrows indicated the capacity loss percentage for each half-cell after 200 cycles. (c) Discharge capability under different C-rate from 2.8 to 4.3 V.

Table 1
Detailed charge–discharge data of each as-prepared sample.

Unit ($mAh{\cdot}g^{-1}$)	NCM811	1 % STO-811	3 % STO-811	5 % STO-811
Initial charge capacity at 0.1C	253.3	235.2	224.9	215.8
Initial discharge capacity at 0.1C	214.9	213.7	207.3	198.2
Initial coulombic efficiency	84.8 %	90.9 %	92.2 %	91.8 %
Discharge capacity at 1C (1st cycle)	200.2	196.7	193.1	184.5
Discharge capacity at 1C (200th cycle)	130.8	140.6	173.5	153.5
Capacity loss (percentage)/cycle (after 200 cycles)	0.35 (0.17 %)	0.28 (0.14 %)	0.10 (0.05 %)	0.16 (0.08 %)
Capacity retention (after 200 cycles)	65.3 %	71.5 %	89.8 %	83.2 %

STO-coated cathodes maintained more specific capacities compared with the unmodified NCM811 when discharged under high C-rate (greater than1C). Notably, 3 % STO-811 shows the highest rate performance among all measured cells; especially at 10C rate, 3 % STO-811 retained 141.3 $mAh{\cdot}g^{-1}$ on average while others are below 130 $mAh{\cdot}g^{-1}$. The significant improvement of rate capability of 3 % STO-811 is probably due to the formation of Li-Ti-O compounds at the cathode-coating layer interface, which accelerates the Li^+ diffusion kinetics under high-rate [35]. In addition, when the current density returns to 0.1C, the discharge capacity of 3 % STO-811 reserved ~ 98 %, higher than that of 81 % for pristine NCM811, which is mainly attributed to the mitigation of interior phase transformation of NCM811 caused by the severe Li^+/Ni^{2+} distortion at a high rate.

To further investigate the influence of the STO surface modification on the inner redox reactions of the NCM811 cathode, CV curves of 3 % STO-811 and the uncoated sample were recorded with a scan rate of 0.1 $mV{\cdot}s^{-1}$. The similar CV features between the pristine NCM811 and 3 % STO-811 suggest that the electrochemical reactions of the NCM811 are not affected by the STO coating; the corresponding phase transition peaks during the charging process are labelled in **Figure S7**. The potential difference (ΔV) between redox peaks is related to the polarization degree of the cathode and the reversibility of its electrochemical reactions [36].

The unmodified NCM811 exhibits a larger ΔV of 0.44 V after the first scan cycle from 2.8 to 4.3 V, demonstrating low electrochemical reversibility induced by high polarization; meanwhile, the 3 % STO-811 displays a smaller ΔV of 0.25 V in the initial scan with well-overlapped sequent CV curves, inferring that the STO-coated NCM811 has excellent reversible Li^+ intercalation/deintercalation kinetics. The differential curves (dQ/dV) are plotted in Fig. 5**(a) and (b)** to deeply evaluate the charging and discharging process of NCM811 and 3 % STO-811. Generally, the oxidation and reduction peaks in the curve correspond to the charging and discharging plateaus correspond to the reactions among Ni^{2+}, Ni^{3+}, and Ni^{4+} [37]. The three oxidation peaks (labelled in Fig. 5**(a)**) reveal the transitions from the hexagonal phase 1 to the monoclinic phase (H1-M), then to another hexagonal phase 2 (M−H2), and finally transferred to the hexagonal phase 3 (H2-H3), respectively. Similar to the CV profiles, the redox peak differences (ΔE) are also related to these phase transitions' reversibility [38]. The strongest oxidation peak of uncoated NCM811 at the initial lies at 3.66 V, and its corresponding reduction peak is located at 3.71 V. The ΔE of the pristine NCM811 is 0.05 V, which is higher than that of 3 % STO-811 (0.02 V), indicating that STO modification can inhibit the polarization during the electrochemical reactions. Thus, 3 % STO-811 could present a more reversible phase transformation during the charge–discharge processes. Besides, the redox peaks shift in the dQ/dV profile is usually associated with capacity degradation and voltage decay of Ni-rich cathode materials, which is linked to the difficulty levels of Li^+ intercalation/deintercalation origin from the structural changes in the Ni-rich oxides [39]. Obviously, the 3 % STO-811 demonstrated a more stable discharge behaviour by showing slower peaks shift tendency than the pristine NCM811 at the 1C rate, especially in the first 50 cycles. Compared to the 0.16 V voltage decay of bare NCM811 after 200 cycles at 1C, the 3 % STO coated NCM811 cathode exhibits a relieved voltage degradation and improved reversibility. The CV and dQ/dV results double confirmed that the STO surface coating could enhance the phase stability and electrochemical reversibility of the NCM811 cathode, which is in agreement with the excellent cyclability and high-rate performance results of the 3 % STO-811.

Electrochemical impedance spectroscopy (EIS) is an effective method to disclose the kinetics and can be quantitatively analysed to approximate the lithium-ion diffusion coefficient ($D(Li^+)$). The EIS spectra of the pristine NCM811 and 3 % STO-811 cathodes were measured after both 1 and 100 cycles at 25 °C. The Nyquist curves were fitted with an equivalent circuit model (inset of Fig. 6**(a)**) and the corresponding data are listed in **Table S2**. Fig. 6**(a)** shows that all the fitting outcomes contain two semicircles: the first semicircle at the high-frequency is associated with CEI film resistance (R_s), and the second semicircle in the medium-frequency represents the charge-transfer resistance (R_{ct}) [40]. Furthermore, the $D(Li^+)$ of the uncoated NCM811 and 3 % STO-811 was calculated by equation (1):

$$D = \frac{R^2T^2}{2A^2n^4F^4C^2\sigma^2} \quad (1)$$

where R is the gas constant (8.314 $J{\cdot}k^{-1}{\cdot}mol^{-1}$), T is the measurement temperature (298.15 K), A is the surface area of the cathode material (~1.54 cm^2), n is the number of transferred charges per unit during the electrochemical reactions (n = 1), F is the Faraday constant (96486C$\cdot mol^{-1}$), C is the Li^+ concentration in the cathode materials (C: ~0.0235 mol$\cdot cm^{-3}$), and σ is the Warburg coefficient, which obeys the equation (2):

$$Z\prime = R_e + R_{ct} + \sigma\omega^{-1/2} \quad (2)$$

where Z' denotes the real part of impedance, R_e is the electrolyte resistance, and ω is the angle frequency ($\omega = 2\pi f$) [17]. The relationship between Z' and $\omega^{-1/2}$ in the low-frequency is shown in Fig. 6**(b)**. The linear fitting slope reflects the Warburg coefficient of each cathode after 1 and 100 cycles.

It can be found that Re for both cathodes after the initial cycle exhibited a similar value due to the approximately same volume of $LiPF_6$ electrolyte utilized during half-cell assembling. After 200 cycles, a slight increase in Re could be stemmed from the electrolyte consumption and inevitable decomposition with a trace amount of water [41]. Both R_s and R_{ct} values of 3 % STO-811 are larger than uncoated NCM811 after the initial cycle, which should be attributed to the STO coating layer is electrochemical inert for Li^+ transfer kinetics when compared to the initially thin CEI layer generated on the cathode surface [42]. After 100 charge–discharge cycles, inevitable side reactions occurred around the pristine NCM811 to generate a thicker CEI layer, dramatically increasing the R_s and R_{ct} values of the bare cathode (R_s and R_{ct} increased more than 10 times and 8 times, respectively). At the same time, the R_{ct} of the 3 % STO-811 sample exhibits a retard growth because of the homogeneous STO protection. Lower R_{ct} also suggests the improved kinetic activity of 3 % STO-811, which can explain the better cyclic stability and rate performance than pristine NCM811. Notably, the existence of the fast ion-conductor (LTO) in the STO-NCM811 interface is probably another reason for the enhanced Li^+ diffusion kinetics.

Moreover, although the obtained $D(Li^+)$ of NCM811 (3.06 × 10^{-13} $cm^2{\cdot}s^{-1}$) after the first cycle is higher than that of the STO coated

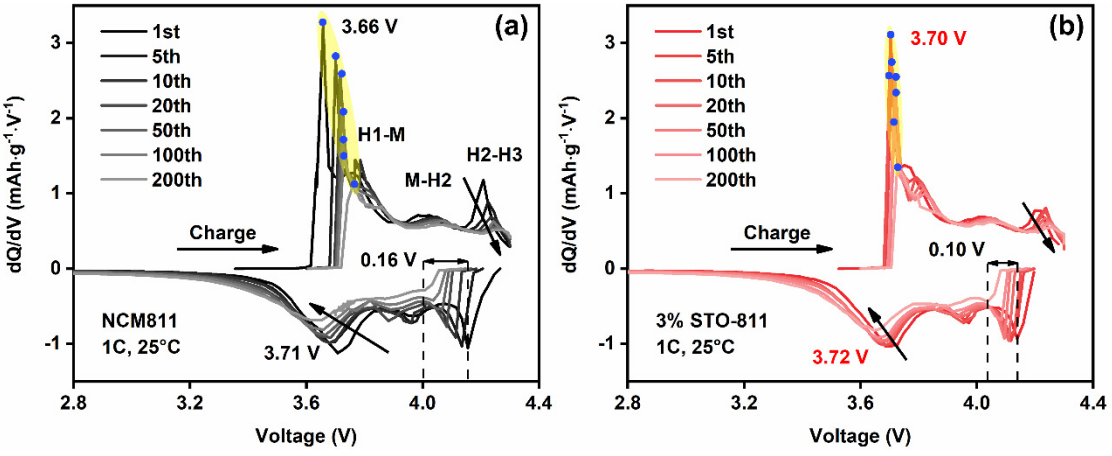

Fig. 5. The dQ/dV curves of the (a) pristine NCM811 and (b) 3 % STO-811 at 1C from 2.8 to 4.3 V.

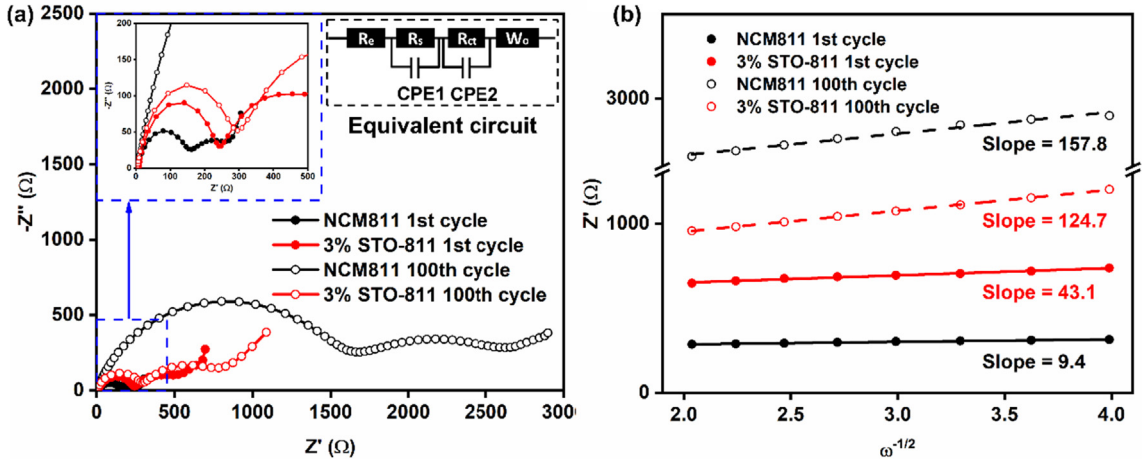

Fig. 6. (a) EIS spectra of pristine NCM811 and 3% STO-811 after initial and 100 cycles. (b) The linear fitting relationship between Z' and $\omega^{-1/2}$.

sample, it quickly fell to 1.08 × 10^{-15} $cm^2 \cdot s^{-1}$ after 100 cycles (decreased more than 35 times), while the 3 % STO-811 maintained a $D(Li^+)$ of 1.74 × 10^{-15} $cm^2 \cdot s^{-1}$, which is 1.6 times higher than the pristine NCM811. The comparison of $D(Li^+)$ variation suggested that the STO coating may play a critical role in suppressing electrolyte decomposition, inhibiting TM dissolution, and hindering CEI formation [43]. The EIS analysis results agree well with the electrochemical measurements, indicating that the STO surface modification could helpfully enhance the electrochemical stability of the Ni-rich cathode material.

To unravel the morphological evolution and microcrack generation inside the cycled cathode particles, unmodified and 3 % STO coated NCM811 materials after 100 charge–discharge cycles were collected from disassembled half cells and post-FIB images are displayed in Fig. 7. It can be recognised from Fig. 7 **(a)** clearly that microcracks originated in the centre of the NCM811 particle after 100 charge–discharge cycles, which are triggered by the phase transition caused crystal contraction and expansion during charge–discharge circulations. The observation is not unforeseen because these cracks induce cathode fissures, cause poor conductions, and expose more facets to the electrolyte, leading to electrochemical performance decay of NCM811 [44]. However, a uniform surface protective layer was generated on the modified NCM811, which could not only mitigate the Ni-rich oxide from HF corrosion but also maintain the structural integrity of the cathode material, as shown in Fig. 7**(b)**.

3.3. In-air storage stability evaluation

According to previous literatures, the in-air storage stability of $LiNiO_2$-based materials has received considerable concerns due to the generation of Li_2CO_3/$LiHCO_3$ on the cathode surface, which has been regarded as the main reason for the performance degradation of Ni-rich cathode after long-term in-air storage [45]. Commonly, excessive Li source was added during the synthesis procedure of Ni-rich cathode to avoid the Li loss at high sintering temperature with oxygen flow, which may cause surface enriched lithium on the cathode particles [46]. This lithium residual on the cathode surface accompanied by the deintercalated Li^+ in NCM811 easily reacts with H_2O and CO_2 in the air, resulting in the specific capacity decrease and cell resistance growth, further decreasing the rate capability [47]. The reaction formulas are described as follows (TM = Ni, Co, and Mn):

$$LiTMO_2 \rightarrow 1/(1+x)\, Li_{1-x}(TM)_{1+x}O_2 + x/(1+x)\, Li_2O + x/2(1+x)O_2 \quad (3)$$

$$LiTMO_2 + (y/2)\, H_2O \rightarrow Li_{1-y}TMO_{2-(y/2)} + y\, LiOH \quad (4)$$

$$LiTMO_2 + (z/2)\, CO_2 \rightarrow Li_{1-z}NiO_{2-z} + (z/2)\, Li_2CO_3 + (z/4)\, O_2 \quad (5)$$

$$LiOH + CO_2 \rightarrow LiHCO_3 \leftrightarrow 1/2\, Li_2CO_3 + 1/2\, CO_2 + 1/2\, H_2O \quad (6)$$

The irreversible decomposition of lithium residual together with gas release during the charging process have been noted and these may induce the battery distention and raise safety problems [48]. The active oxygen species aroused side effects that would also lead to conversion from Ni^{3+} to Ni^{2+} in Ni-rich NCM811, increasing the probability of Li/Ni cation mixing and causing severe capacity fading [49]. **Figure S8(a, b)** shows the

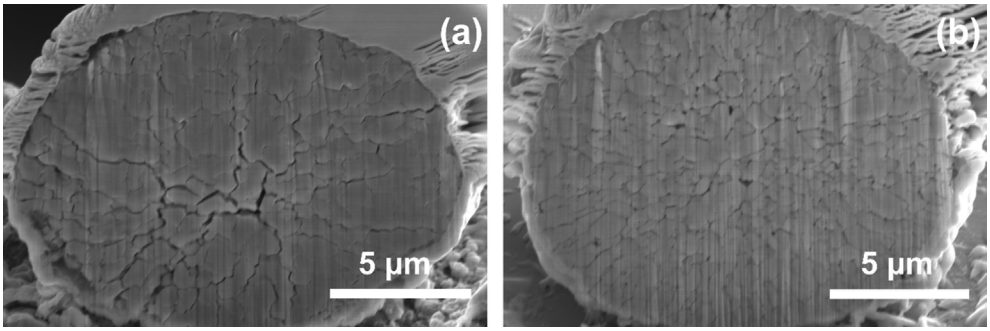

Fig. 7. FIB images of (a) pristine NCM811 and (b) 3% STO-811 cathode particles after 100 cycles.

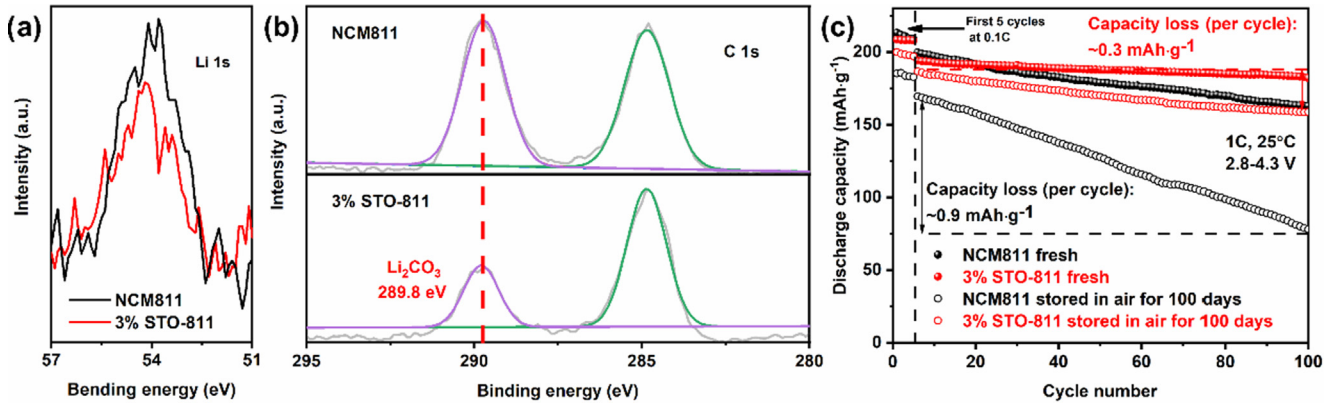

Fig. 8. (a) XPS Li 1 s and (b) C 1 s spectra of NCM811 and 3 % STO-811 after 100 days in-air storage. (c) cyclic data of fresh and 100 days in-air stored cathode samples.

SEM images of the NCM811 and 3 % STO-811 stored in the air after 100 days. Compared with the freshly as-synthesized samples illustrated in Fig. 1**(b) and (d)**, small dots appear on the surface of bare NCM811 particles after being stored in air for 100 days, while the 3 % STO exhibits unchanged surface conditions. Fig. 8**(a)** compares the XPS Li 1 s curves between the NCM811 and 3 % STO-811 stored in the air after 100 days, displaying a similar peak position. It is reasonable that the STO coating layer slightly reduced the peak intensity due to the covered cathode surface. XPS C 1 s spectra exhibit both characteristic peaks located at 284.8 eV and 289.8 eV (Fig. 8**(b)**), in which the 289.8 eV characteristic peak is an indication of Li_2CO_3 [50]. The intensity of the Li_2CO_3 peak for the STO modified NCM811 stored in the air after 100 days is significantly reduced, suggesting that the Li_2CO_3 generation on the cathode surface may be suppressed. Combining the SEM and XPS results indicated that the protective STO coating layer on the cathode particle surface could effectively isolate the bulk material from H_2O and CO_2 when stored in the air. Fig. 8 **(c)** illustrates the charge–discharge curves of the fresh and in-air stored NCM811 cathode materials with and without STO surface nanocoating. The black and red dots represent the 100 charge–discharge cycles of fresh NCM811 and 3 % STO-811 from 2.8 to 4.3 V at 1C, respectively. The fresh samples reveal almost the same trends as the previous presented cyclic performances, confirming that the surface modification strategy is reproducible and trustworthy. After 100 days of in-air storage, the bare NCM811 displays poor cyclicality. On the one hand, the initial discharge capacity decreased to 185.3 $mAh{\cdot}g^{-1}$ at 0.1C, which is lower than the fresh NCM811 (213.3 $mAh{\cdot}g^{-1}$) because of the inactive Li_2CO_3 formed on the cathode surface. On the other hand, its discharge capacity quickly dropped from 169.5 to 78.1 $mAh{\cdot}g^{-1}$ with only a capacity retention of ~ 46 % after 100 cycles at 1C. Even though the initial discharge capacity of 3 % STO-811 also reduced from 208.7 to ~ 200 $mAh{\cdot}g^{-1}$ at 0.1C, its capacity preserved ~ 85 % (from 186.7 to 158.8 $mAh{\cdot}g^{-1}$) after 100 cycles, which is still higher than the fresh NCM811 (~81 %). The enhanced initial discharge capacity and improved capacity retention of in-air stored 3 % STO-811 compared with bare NCM811 strongly prove that the STO surface modification could prolong the in-air storage life of Ni-rich cathode materials.

4. Conclusion

Strontium titanate, a typical perovskite oxide is firstly introduced as a surface modifier into popular Ni-rich layered $LiNi_{0.8}Co_{0.1}Mn_{0.1}O_2$ cathode. Thin and homogeneous STO-coated NCM811 cathode were obtained through a facile wet chemical process, which showed improved electrochemical performances. The optimized 3 wt% STO coated NCM811 sample exhibited an excellent cyclic stability with ~ 90 % capacity retention after 200 cycles at 1C, which indicated only 0.05 % capacity loss per cycle. The enhanced cycling performance was ascribed to the uniform STO nanocoating that could effectively suppress the side reactions between the Ni-rich cathode and the organic electrolyte. On the other hand, the STO coating layer maintained the interior structure integrity of cathode particles, increased the stability of reversible redox reactions, and reduced the polarization during the charge–discharge process at high current density. Additionally, the STO coated NCM811 could also mitigate the Li_2CO_3 generation on the cathode surface by effective isolation from H_2O and CO_2, and thus higher specific capacity was retained after long-term storage in air compared to the uncoated NCM811 sample. Our studies proposed an effective surface modification strategy to enhance the electrochemical performance of layered ternary oxides for high performance-cathodes in commercial LIBs.

CRediT authorship contribution statement

Peiyuan Guan: Writing – original draft, Investigation, Formal analysis. **Yanzhe Zhu:** Investigation, Data curation. **Mengyao Li:** Formal analysis, Data curation. **Tianyi Zeng:** Formal analysis. **Xiaowei Li:** Writing – review & editing. **Ruoming Tian:** Formal analysis. **Neeraj Sharma:** Resources, Writing – review & editing. **Zhemi Xu:** Validation, Data curation. **Tao Wan:** Investigation, Writing – review & editing. **Long Hu:** Writing – review & editing. **Yunjian Liu:** Resources, Methodology. **Claudio Cazorla:** Writing – review & editing. **Dewei Chu:** Supervision, Conceptualization, Funding acquisition.

Data availability

Data will be made available on request.

Declaration of Competing Interest

The authors declare that they have no known competing financial interests or personal relationships that could have appeared to influence the work reported in this paper.

Acknowledgments

P. Guan would like to thank the financial support from Research Training Program (RTP) funded by the Department of Education, Australia. D. Chu and N. Sharma acknowledges financial support

from the Australian Research Council (LP1900113). The authors also would like to acknowledge the Mark Wainwright Analytical Centre at UNSW Sydney for access to X-ray diffraction and mass spectrometry facilities.

Appendix A. Supplementary data

Supplementary data to this article can be found online at https://doi.org/10.1016/j.jcis.2022.08.061.

References

[1] Y. Liu et al., Coating ultra-thin TiN layer onto LiNi0.8Co0.1Mn0.1O2 cathode material by atomic layer deposition for high-performance lithium-ion batteries, J. Alloy. Compd. 888 (2021) 161594.
[2] X. Liu et al., Stabilizing the high-voltage cycle performance of LiNi0.8Co0.1Mn0.1O2 cathode material by Mg doping, J. Power Sources 438 (2019) 227017.
[3] F. Schipper, H. Bouzaglo, M. Dixit, E.M. Erickson, T. Weigel, M. Talianker, J. Grinblat, L. Burstein, M. Schmidt, J. Lampert, C. Erk, B. Markovsky, D.T. Major, D. Aurbach, From Surface ZrO2 Coating to Bulk Zr Doping by High Temperature Annealing of Nickel-Rich Lithiated Oxides and Their Enhanced Electrochemical Performance in Lithium Ion Batteries, Adv. Energy Mater. 8 (4) (2018) 1701682.
[4] S. Yin, W. Deng, J. Chen, X.u. Gao, G. Zou, H. Hou, X. Ji, Fundamental and solutions of microcrack in Ni-rich layered oxide cathode materials of lithium-ion batteries, Nano Energy 83 (2021) 105854.
[5] J. Cui, X. Ding, D. Luo, H. Xie, Z. Zhang, B. Zhang, F. Tan, C. Liu, Z. Lin, Effect of Cationic Uniformity in Precursors on Li/Ni Mixing of Ni-Rich Layered Cathodes, Energy Fuels 35 (2) (2021) 1842–1850.
[6] P. Mukherjee, P. Lu, N. Faenza, N. Pereira, G. Amatucci, G. Ceder, F. Cosandey, Atomic Structure of Surface-Densified Phases in Ni-Rich Layered Compounds, ACS Appl. Mater. Interfaces 13 (15) (2021) 17478–17486.
[7] L. Song, A. Li, Z. Xiao, Z. Chi, Z. Cao, H. Zhu, Enhanced electrochemical properties of Ni-rich LiNi0.8Co0.1Mn0.1O2 by SnO2 coating under high cutoff voltage, Ionics 26 (6) (2020) 2681–2688.
[8] Q. Lin, W. Guan, J. Meng, W. Huang, X. Wei, Y. Zeng, J. Li, Z.e. Zhang, A new insight into continuous performance decay mechanism of Ni-rich layered oxide cathode for high energy lithium ion batteries, Nano Energy 54 (2018) 313–321.
[9] Y.-Y. Sun, S. Liu, Y.-K. Hou, G.-R. Li, X.-P. Gao, In-situ surface modification to stabilize Ni-rich layered oxide cathode with functional electrolyte, J. Power Sources 410-411 (2019) 115–123.
[10] Q. Wu, S. Mao, Z. Wang, Y. Tong, Y. Lu, Improving LiNixCoyMn1−x−yO2 cathode electrolyte interface under high voltage in lithium ion batteries, Nano Select 1 (1) (2020) 111–134.
[11] J. Zhu, Y. Li, L. Xue, Y. Chen, T. Lei, S. Deng, G. Cao, Enhanced electrochemical performance of Li3PO4 modified Li[Ni0.8Co0.1Mn0.1]O2 cathode material via lithium-reactive coating, J. Alloy. Compd. 773 (2019) 112–120.
[12] Y. Zhai, W. Yang, D.e. Ning, J. Yang, L. Sun, G. Schuck, G. Schumacher, X. Liu, Improving the cycling and air-storage stability of LiNi0.8Co0.1Mn0.1O2 through integrated surface/interface/doping engineering, J. Mater. Chem. A 8 (10) (2020) 5234–5245.
[13] Y. Huang, X. Yao, X. Hu, Q. Han, S. Wang, L.-X. Ding, H. Wang, Surface coating with Li-Ti-O to improve the electrochemical performance of Ni-rich cathode material, Appl. Surf. Sci. 489 (2019) 913–921.
[14] P. Guan, L.u. Zhou, Z. Yu, Y. Sun, Y. Liu, F. Wu, Y. Jiang, D. Chu, Recent progress of surface coating on cathode materials for high-performance lithium-ion batteries, Journal of Energy Chemistry 43 (2020) 220–235.
[15] P. Lupetin, G. Gregori, J. Maier, Mesoscopic Charge Carriers Chemistry in Nanocrystalline SrTiO3, Angew. Chem. Int. Ed. 49 (52) (2010) 10123–10126.
[16] Y.A. Hao, X.H. Wang, L.T. Li, Highly dispersed SrTiO3 nanocubes from a rapid sol-precipitation method, Nanoscale 6 (14) (2014) 7940–7946.
[17] X. Zhang, P. Zhang, T. Zeng, Z. Yu, X. Qu, X. Peng, Y.u. Zhou, X. Duan, A. Dou, M. Su, Y. Liu, Improving the Structure Stability of LiNi0.8Co0.15Al0.05O2 by Double Modification of Tantalum Surface Coating and Doping, ACS Applied Energy Materials 4 (8) (2021) 8641–8652.
[18] T. Wu, G. Wang, B. Liu, Q. Huang, Y. Su, F. Wu, R.M. Kelly, The role of Cu impurity on the structure and electrochemical performance of Ni-rich cathode material for lithium-ion batteries, J. Power Sources 494 (2021) 229774.
[19] W. Xiang, W.-Y. Liu, J. Zhang, S. Wang, T.-T. Zhang, K. Yin, X.i. Peng, Y.-C. Jiang, K.-H. Liu, X.-D. Guo, Controlled synthesis of nickel-rich layered oxide cathodes with preferentially exposed 010 active facets for high rate and long cycling stable lithium-ion batteries, J. Alloy. Compd. 775 (2019) 72–80.
[20] P. Guan et al., Performance degradation and mitigation strategies of silver nanowire networks: a review, Crit. Rev. Solid State Mater. Sci. (2021) 1–25.
[21] W.F. Goh, T.L. Yoon, S.A. Khan, Molecular dynamics simulation of thermodynamic and thermal transport properties of strontium titanate with improved potential parameters, Comput. Mater. Sci. 60 (2012) 123–129.
[22] J. Zhu, S. Sharifi-Asl, J.C. Garcia, H.H. Iddir, J.R. Croy, R. Shahbazian-Yassar, G. Chen, Atomic-Level Understanding of Surface Reconstruction Based on Li [NixMnyCo1-x-y]O-2 Single-Crystal Studies, Acs Applied Energy Materials 3 (5) (2020) 4799–4811.
[23] H.H. He et al., Feasible synthesis of NCM811 cathodes with controllable Li/Ni cationic mixing for enhanced electrochemical performance via a nano grinding assisted solid-state approach, Int. J. Energy Res. 45 (5) (2021) 7108–7119.
[24] T. Wang, K. Ren, W. Xiao, W. Dong, H. Qiao, A. Duan, H. Pan, Y. Yang, H. Wang, Tuning the Li/Ni Disorder of the NMC811 Cathode by Thermally Driven Competition between Lattice Ordering and Structure Decomposition, J. Phys. Chem. C 124 (10) (2020) 5600–5607.
[25] H. Liu, Y. Yang, J. Zhang, Investigation and improvement on the storage property of LiNi0.8Co0.2O2 as a cathode material for lithium-ion batteries, J. Power Sources 162 (1) (2006) 644–650.
[26] F. Schipper, M. Dixit, D. Kovacheva, M. Talianker, O. Haik, J. Grinblat, E.M. Erickson, C. Ghanty, D.T. Major, B. Markovsky, D. Aurbach, Stabilizing nickel-rich layered cathode materials by a high-charge cation doping strategy: zirconium-doped LiNi0.6Co0.2Mn0.2O2, J. Mater. Chem. A 4 (41) (2016) 16073–16084.
[27] T. Weigel, F. Schipper, E.M. Erickson, F.A. Susai, B. Markovsky, D. Aurbach, Structural and Electrochemical Aspects of LiNi0.8Co0.1Mn0.1O2 Cathode Materials Doped by Various Cations, ACS Energy Lett. 4 (2) (2019) 508–516.
[28] X. Qu, Z. Yu, D. Ruan, A. Dou, M. Su, Y.u. Zhou, Y. Liu, D. Chu, Enhanced Electrochemical Performance of Ni-Rich Cathode Materials with Li1.3Al0.3Ti1.7(PO4)(3) Coating, ACS Sustainable Chem. Eng. 8 (15) (2020) 5819–5830.
[29] K.Y. Li, D.F. Xue, Estimation of electronegativity values of elements in different valence states, J. Phys. Chem. A 110 (39) (2006) 11332–11337.
[30] H. Kim, J. Jang, D. Byun, H.-S. Kim, W. Choi, Selective TiO2 Nanolayer Coating by Polydopamine Modification for Highly Stable Ni-Rich Layered Oxides, ChemSusChem 12 (24) (2019) 5253–5264.
[31] X. Pan, Y. Shuai, C. Wu, W. Luo, X. Sun, H. Zeng, X. Bai, C. Gong, K.e. Jian, L.u. Zhang, H. Guo, B. Tian, W. Zhang, Switchable diode effect in oxygen vacancy-modulated SrTiO3 single crystal, Applied Physics a-Materials Science & Processing 123 (9) (2017).
[32] J.-Y. Baek, L.T. Duy, S.Y. Lee, H. Seo, Aluminum doping for optimization of ultrathin and high-k dielectric layer based on SrTiO3, J. Mater. Sci. Technol. 42 (2020) 28–37.
[33] K. Mukai, M. Yashima, K. Hibino, T. Terai, Experimental Visualization of Interstitialcy Diffusion of Li Ion in β-Li2TiO3, ACS Applied Energy Materials 2 (8) (2019) 5481–5489.
[34] H. Yu, Y. Cao, L. Chen, Y. Hu, X. Duan, S. Dai, C. Li, H. Jiang, Surface enrichment and diffusion enabling gradient-doping and coating of Ni-rich cathode toward Li-ion batteries, Nat. Commun. 12 (1) (2021).
[35] E. Hu, X. Wang, X. Yu, X.-Q. Yang, Probing the Complexities of Structural Changes in Layered Oxide Cathode Materials for Li-Ion Batteries during Fast Charge-Discharge Cycling and Heating, Acc. Chem. Res. 51 (2) (2018) 290–298.
[36] Y. Liu, L.-b. Tang, H.-X. Wei, X.-H. Zhang, Z.-J. He, Y.-J. Li, J.-C. Zheng, Enhancement on structural stability of Ni-rich cathode materials by in-situ fabricating dual-modified layer for lithium-ion batteries, Nano Energy 65 (2019) 104043.
[37] T. Li, D. Li, Q. Zhang, J. Gao, L. Zhang, X. Liu, Improving Fast Charging-Discharging Performances of Ni-Rich LiNi0.8Co0.1Mn0.1O2 Cathode Material by Electronic Conductor LaNiO3 Crystallites, Materials 15 (1) (2022) 396.
[38] H. Yang, H.-H. Wu, M. Ge, L. Li, Y. Yuan, Q.i. Yao, J. Chen, L. Xia, J. Zheng, Z. Chen, J. Duan, K. Kisslinger, X.C. Zeng, W.-K. Lee, Q. Zhang, J. Lu, Simultaneously Dual Modification of Ni-Rich Layered Oxide Cathode for High-Energy Lithium-Ion Batteries, Adv. Funct. Mater. 29 (13) (2019) 1808825.
[39] M. Jiang, D.L. Danilov, R.-A. Eichel, P.H.L. Notten, A Review of Degradation Mechanisms and Recent Achievements for Ni-Rich Cathode-Based Li-Ion Batteries, Adv. Energy Mater. 11 (48) (2021) 2103005.
[40] M.A. Razmjoo Khollari, M.K. Azar, M. Esmaeili, N. Malekpour, S.M. Hosseini-Hosseinabad, R.S. Moakhar, A. Dolati, S. Ramakrishna, Electrochemical Performance and Elevated Temperature Properties of the TiO2-Coated Li[Ni0.8Co0.1Mn0.1]O2 Cathode Material for High-Safety Li-Ion Batteries, ACS Applied Energy Materials 4 (5) (2021) 5304–5315.
[41] S. Wen, Y. Han, P. Wang, D. Zhao, X. Cui, L. Zhang, S. Li, An Interfacial Mechanism of Chelate-Borate Electrolyte Additives in Ni-Rich LiNi0.8Mn0.1Co0.1O2 Cathodes, Acs Applied Energy Materials 4 (11) (2021) 12525–12534.
[42] W. Cho, S.-M. Kim, J.H. Song, T. Yim, S.-G. Woo, K.-W. Lee, J.-S. Kim, Y.-J. Kim, Improved electrochemical and thermal properties of nickel rich LiNi0.6Co0.2Mn0.2O2 cathode materials by SiO2 coating, J. Power Sources 282 (2015) 45–50.
[43] H. Yang, K.e. Du, G. Hu, Z. Peng, Y. Cao, K. Wu, Y. Lu, X. Qi, K. Mu, J. Wu, Graphene@TiO2 co-modified LiNi0.6Co0.2Mn0.2O2 cathode materials with enhanced electrochemical performance under harsh conditions, Electrochim. Acta 289 (2018) 149–157.
[44] Q. Fan, K. Lin, S. Yang, S. Guan, J. Chen, S. Feng, J. Liu, L. Liu, J. Li, Z. Shi, Constructing effective TiO2 nano-coating for high-voltage Ni-rich cathode materials for lithium ion batteries by precise kinetic control, J. Power Sources 477 (2020) 228745.
[45] Y.a. You, H. Celio, J. Li, A. Dolocan, A. Manthiram, Modified High-Nickel Cathodes with Stable Surface Chemistry Against Ambient Air for Lithium-Ion Batteries, Angewandte Chemie-International Edition 57 (22) (2018) 6480–6485.
[46] Y. Bi, T. Wang, M. Liu, R. Du, W. Yang, Z. Liu, Z. Peng, Y. Liu, D. Wang, X. Sun, Stability of Li2CO3 in cathode of lithium ion battery and its influence on electrochemical performance, RSC Adv. 6 (23) (2016) 19233–19237.

[47] Y. Kim, H. Park, K. Shin, G. Henkelman, J.H. Warner, A. Manthiram, Rational Design of Coating Ions via Advantageous Surface Reconstruction in High-Nickel Layered Oxide Cathodes for Lithium-Ion Batteries, Adv. Energy Mater. 11 (38) (2021) 2101112.
[48] S.W. Doo, S. Lee, H. Kim, J.H. Choi, K.T. Lee, Hydrophobic Ni-Rich Layered Oxides as Cathode Materials for Lithium-Ion Batteries, Acs Applied Energy Materials 2 (9) (2019) 6246–6253.
[49] N. Mahne, S.E. Renfrew, B.D. McCloskey, S.A. Freunberger, Electrochemical Oxidation of Lithium Carbonate Generates Singlet Oxygen, Angewandte Chemie-International Edition 57 (19) (2018) 5529–5533.
[50] X. Zhang, J. Xu, X. Liu, F. Cheng, P. Wei, Y. Xu, S. Sun, H.e. Lin, Y. Shen, Q. Li, C. Fang, J. Han, Building a stabilized structure from surface to bulk of Ni-rich cathode for enhanced electrochemical performance, Energy Storage Mater. 47 (2022) 87–97.